Combustion and Flame 232 (2021) 111520

Contents lists available at ScienceDirect

Combustion and Flame

journal homepage: www.elsevier.com/locate/combustflame

Curvature effects on NO formation in wrinkled laminar ammonia/hydrogen/nitrogen-air premixed flames

Corinna Netzer[a,*], Ahfaz Ahmed[a], Andrea Gruber[a,b], Terese Løvås[a]

[a] Department of Energy and Process Engineering, Norwegian University of Science and Technology, Trondheim, Norway
[b] SINTEF Energy Research, Trondheim, Norway

ARTICLE INFO

Article history:
Received 29 June 2020
Revised 20 May 2021
Accepted 20 May 2021

Keywords:
Premixed flames
Wrinkled flames
Flame curvature
NO formation
Hydrogen-nitrogen-ammonia fuel blending

ABSTRACT

The formation of nitrogen oxide (NO) in wrinkled laminar $NH_3/H_2/N_2$-air premixed flames is investigated utilizing two-dimensional Direct Numerical Simulation (DNS) with detailed chemical kinetics as well as one-dimensional freely propagating flame calculations. The spatial pattern of NO formation is observed to be closely linked to flame curvature and affected by thermo-diffusive effects acting on key chemical species. Preferential diffusion of H_2 into convex-shaped portions of the flame front leads to a local increase in equivalence ratio. This change in local equivalence ratio is found to prominently affect the NO formation. If the fuel-oxidant mixture is globally lean, a local increase in equivalence ratio strengthens the NO formation (locally); in a globally rich fuel-oxidant mixture, conversely, the NO concentration will be reduced in correspondence of local increments of the equivalence ratio. A sensitivity analysis with respect to NO formation reveals that decomposition of NH_2 is governed by two competing pathways: the decomposition via NH and N to N_2 on the one hand and the oxidation via HNO to NO on the other hand. The local radical pool, which is affected by preferential diffusion of H_2 and depletion of O_2, and the local fuel-oxidant mixture ratio jointly strengthen further local differences between H_2-depleted (concave-shaped) portions of the flame front and H_2-enriched (convex-shaped) ones. This is confirmed across a wide range of equivalence ratios from lean to rich conditions.

1. Introduction

Hydrogen (H_2) represents the simplest and one of the cleanest energy carrier for large scale thermal energy conversion and its widespread deployment in the energy sector, if realized, represents one of the most promising strategies to reduce the dependence on fossil fuels and simultaneously reduce atmospheric pollution. This applies both to power generation with pre-combustion carbon sequestration, where hydrogen is produced e.g. at large scale from natural gas in conjunction with carbon dioxide capture and storage [1], and to large-scale energy-storage schemes, where hydrogen is produced from water electrolysis using intermittent excess power from non-dispatchable renewable energy sources (wind, sun) [2]. In the context of large-scale and long-term (seasonal) energy transport and storage, refining hydrogen to ammonia (NH_3), as a convenient carbon-free energy carrier, constitutes a viable and economic alternative to liquefied or highly compressed hydrogen. This is due to the fact that, at moderate pressure, the higher boiling temperature of ammonia compared to hydrogen greatly simplifies its transportation and storage in liquid phase. While the energy penalty of ammonia synthesis from H_2 and nitrogen (N_2) [3] compares with that of the hydrogen liquefaction process, the energy density of ammonia exceeds that of liquid hydrogen by 57% (3.724 MWh/m^3 versus 2.368 MWh/m^3, respectively). Furthermore, due to the widespread utilisation of ammonia in agriculture and as refrigerant, commercial technologies are already in place for production, transportation and storage of ammonia with an excellent safety record despite its characteristic toxicity.

The presence of a considerable differences between the combustion properties of ammonia and methane (conservatively considered here as a lower-reactivity representative of natural gas) implies that burner design necessarily becomes rather sub-optimal in respect to the exploration of fuel flexibility in gas turbines. While early studies have indicated an obvious inadequacy of neat ammonia as a gas turbine fuel due to its poor reactivity compared to conventional hydrocarbons [4], a significant number of studies has been published on combustion of hydrogen/ammonia with air (e.g. [5]) or hydrogen/ammonia/methane with air (e.g. [6] in order to mitigate the low reactivity of neat ammonia. Also, a number of

* Corresponding author.
E-mail address: corinna.netzer@ntnu.no (C. Netzer).

https://doi.org/10.1016/j.combustflame.2021.111520

more recent studies based on rich-lean fuel staging have shown encouraging results [7,8]. Combustion tests with fuel blends consisting of mixtures of ammonia and hydrogen are indeed under investigation within industrial demonstration framework[1] In this context, it is interesting to note that partial cracking of ammonia, to form opportunely selected fuel mixtures of ammonia, hydrogen and nitrogen, has a good potential to improve the overall reactivity of the fuel and its combustion performance rendering it more suitable to gas turbines originally designed for use with natural gas. Production of nitrogen oxide (NO) through fuel chemistry in the combustion of ammonia and ammonia-containing fuel blends often is, however, a detriment requiring a detailed study of its formation mechanism with the ultimate objective of obtaining combustor design guidelines for its mitigation.

Recent studies from the open literature also found that, in ammonia combustion, a more prominent impact on the formation of NO is caused by the equivalence ratio in respect to thermal effects, however all of these earlier studies discuss global rather than local differences in the equivalence ratio. Sabia et al. [9] investigated the NO formation in NH_3/air-mixtures as function of inlet temperature and equivalence ratio in a jet stirred flow reactor. They concluded that NO formation is strongly affected by the equivalence ratio with increasing dependency on higher temperatures. Sorrentino et al. [10], from their cyclonic burner measurements of ammonia conversion in the mild combustion regime, concluded that a major impact of the stoichiometry on NO formation at various inlet temperatures and nominal thermal powers is present. Likewise, the papers by Somarathne et al. [11] and Okafor et al. [12], suggest that, due to the strong dependency of NO formation on equivalence ratio for gas turbines, a two-stage rich-lean concept is favourable to control the NO formation in NH_3/air-mixtures.

The present work deploys the recently updated nitrogen-chemistry subset of the San Diego mechanism [13] in conjunction with two-dimensional (2-D) Direct Numerical Simulation (DNS) performed with the S3D code [14]. The fundamental characteristics of wrinkled laminar $NH_3/H_2/N_2$-air premixed flames is investigated to quantify and explain NO concentration trends across the relevant range of fuel-oxidant ratios for gas turbine combustion, spanning from fuel-lean to fuel-rich conditions. 2-D DNS, featuring detailed chemical reaction kinetics, is a well-established (and now relatively affordable) numerical modelling approach that has been widely used in past fundamental combustion studies to accurately quantify the local effects of curvature, stretch, Lewis number, pocket formation and consumption, and non-homogeneous distribution of temperature and/or species on the propagation and spontaneous ignition characteristics of wrinkled laminar premixed flames [15–23]. Although the present work does not claim to closely (and rather ambitiously) reproduce the turbulent combustion process taking place in realistic burner geometries at gas turbine conditions, DNS of 2-D geometrically simple flames provides nevertheless useful insight into key, rate-limiting fundamental mechanisms that also take place in more complex flame configurations. These calculations are, as such, relevant to the improved understanding and the further development of industrial combustion applications. In our investigation, adopting the same fundamental methodological approach as in earlier studies, we provide a detailed insight into the spatial patterns of NO formation that take place in wrinkled laminar flames characterized by different global stoichiometric conditions and subject to various degree of strain and curvature, locally in the reaction layer. This is to improve our understanding of the chemical pathways and of their interaction with the characteristic thermo-diffusive instabilities of hydrogen flames, that ultimately lead to different levels of NO formation from combustion of $NH_3/H_2/N_2$-air mixtures. The paper is organized as follows: Section 2 describes the numerical method and the flame configurations simulated, Section 3 presents the DNS results and provides an interpretation based on chemical reaction kinetics considerations, while Section 4 summarizes the present findings and suggests topics for further work.

[1] BIGH2/Phase III - "Enabling safe, clean and efficient utilization of hydrogen and ammonia as the carbon-free fuels of the future" - CLIMIT-Demo Project Number 617137 performed by SINTEF, NTNU, Siemens Industrial Turbomachinery and Equinor ASA.

2. Numerical implementation and simulation details

The S3D code, developed at Sandia National Laboratories [14], is employed to perform the DNS of $NH_3/H_2/N_2$-air premixed flames. The solver discretizes the Navier-Stokes equations for a reactive, multi-component, compressible fluid on a 1024 x 512 Cartesian mesh that covers a rectangular domain of 2 cm x 1 cm, thereby providing a spatial resolution of approximately 20 μm. Spatial derivatives are computed with an eighth-order, explicit, centered, finite-difference scheme (third-order one-sided stencils are used at the domain boundaries in the non-homogeneous directions) in conjunction with a tenth-order, explicit, spatial filter to remove high frequency noise and reduce aliasing error [24]. A fourth-order-accurate, six-stages-explicit, Runge-Kutta algorithm [25] is employed for time integration and the time step is fixed to 5 ns throughout the simulations. The spatial resolution adopted, jointly with the spatial and temporal discretization methods, is sufficient to accurately resolve the flame structure and all diffusive, reactive, and dissipative scales of the target reacting flows, even at the most severe level of stretch applied to the wrinkled flames. The ability of the DNS code to correctly resolve the flame structure results from the combination of the formal numerical order of accuracy of the spatial discretization scheme and of the resolution adopted in the simulations (20 μm), this was verified in a series of one-dimensional unstrained and strained laminar premixed flame DNS calculations (not shown). A mixture-averaged approximation is employed for the diffusion coefficients that are formulated in terms of the binary diffusion coefficients and the mixture composition, where the binary coefficient matrix is symmetric and the diagonal elements are zero. Furthermore, thermal diffusion (the Soret effect) is included in the model formulation for the species diffusion velocities because of its prominent role in mixtures containing hydrogen. Boundary conditions (BC) are periodic (cyclic) in the y-direction, perpendicular to the mean flow of the fresh reactants that enter the domain from the inlet positioned at $x = 0$ cm. The simulations are initialized from a freely propagating planar laminar flame solution through a progress variable (C) mapping that, at the beginning of the time stepping, places a reaction layer of appropriate thickness at $x = 1$ cm (the reaction progress variable C is a parametrization of the flame structure that is equal to 0 in the fresh reactants and 1 in the burnt products). We define the progress variable C using the equilibrium (subscript eq) mass fraction of water for each global equivalence ratio investigated, respectively:

$$C = \frac{Y_{H_2O}}{Y_{H_2O,eq}}. \quad (1)$$

The combustion products exit the computational domain from an outlet placed at $x = 2$ cm. Notably, for the domain inlet and outlet, acoustically non-reflective inflow and outflow boundary conditions are adopted according to the Navier-Stokes characteristic boundary conditions (NSCBC) methodology. The NSCBC implementation in S3D is largely based on the formulation first described by Poinsot and Lele [26] and includes some modifications later suggested for the S3D code specifically [27]. A random 2-D flow field with a prescribed Passot-Pouquet energy spectrum (quantitatively characterized by a rms velocity fluctuation of $u' =$

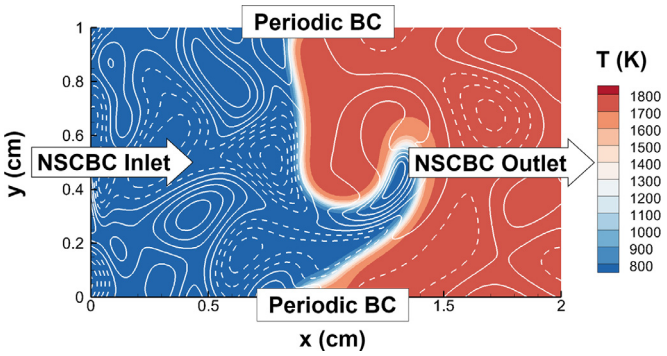

Fig. 1. Illustration of the 2-D computational domain with text labels marking the boundary conditions and color patterns highlighting the instantaneous shape of the wrinkled flame. The lines represent isovalues of z-vorticity (dashed for negative values).

1 m/s and an integral length scale of $L_T = 0.8$ cm) is superimposed onto the mean flow that enters the domain and induces wrinkling of the premixed flame front. The turbulent Reynolds number representative of the pattern of velocity fluctuations that is imposed on the flow field is estimated to be approximately $Re_t \sim 144$. However, it is important to note that the present DNS study is not intended to provide an accurate representation of turbulent flames, whereas the synthetic turbulence is rather used as a mean of achieving a well-characterized wrinkling of the flame front. For the full duration of the time stepping, the mean flow velocity at the inlet boundary is adjusted, at each time step, so that the total amount of fuel that instantaneously enters the domain matches exactly the fuel instantaneously consumed by the combustion process (integrated throughout the computational domain). This procedure warrants that the mean flow velocity is approximately equal to the propagation speed of the wrinkled flame front thereby ensuring that the latter remains within the central portion of the computational domain (approximately). A sketch of the computational setup is provided in Fig. 1 specifying the boundary conditions imposed and highlighting the interaction of the flame front with the 2-D flow field. All of the computations reported here pertain to atmospheric pressure conditions and to a reactants' temperature of 750 K.

The fuel blend mixed with air and introduced at the domain inlet consists of 40% NH_3, 45% H_2 and 15% N_2 (by volume). This specific fuel blend is selected for the present investigation because its combustion in air results in adiabatic flame temperatures T_{ad}, (unstrained) laminar flame thicknesses δ_L and velocities S_L that are very close to typical values observed for combustion of methane (conventional gas turbine fuel) in air [13] (more prominently so at fuel-lean conditions). Accordingly, due to its combustion similarities with methane at relevant conditions, this is considered a good candidate fuel mixture in a targeted search for potential carbon-free drop-in fuels substituting hydrocarbon fuels across a wide range of combustion devices. The present choice, however, does not necessarily imply that this specific mixture represents the most suitable fuel for actual deployment in gas turbines and gas-fired reciprocating engines applications but, in the authors' view, it is rather to be considered as a good starting point. Additionally, in order to complement results from combustion of the target fuel blend, a different fuel blend consisting of 72% NH_3, 21% H_2 and 7% N_2 (by volume) is also included in the present analysis. This is meant as a representative case for the process of partial cracking of ammonia that is conducted to a lower extent, thereby requiring a smaller amount of waste heat from the thermodynamic cycle (gas turbine or internal combustion engine). Extensive validation of all candidate fuel blends will have to include static and dynamic flame stabilization (flashback and combustion dynamics control) and control of pollutants (NO_x, N_2O and NH_3 emissions) and is beyond the objective of the present investigation.

Six different values of the equivalence ratio Φ for the burnable fuel-oxidant mixtures are investigated in the present study, Φ = 0.3, 0.45, 0,8, 0.9, 1.0 and 1.1, spanning from ultra-lean to moderately fuel-rich conditions in order to explore NO formation patterns throughout the stoichiometric range relevant to gas turbine combustors with advanced fuel staging (e.g. Siemens' Rich-Pilot-Lean, or RPL, stage integrated with a second pilot and a main stage [28]). Laminar flame properties for the fuel blends investigated are given in Table 1.

3. Results

3.1. Qualitative features of the flame front

In order to provide a qualitative overview of the spatial patterns observed for key radical species, Figure 2 illustrates the instantaneous flame front, subjected to wrinkling with convex (center of curvature on the products' side of the flame, in the following referred as "convex" or "cx" in later figures) and concave (center of curvature on the reactants' side of the flame, in the following referred as "concave" or "cc" in later figures) characteristic shapes. A considerable variance in the spatial pattern of mass fraction NO is observed in the vicinity of the reaction zone. In the case of very lean mixtures, for Φ = 0.3 and 0.45, the convex-shaped portions of the flame front exhibit higher NO concentration than the concave ones; this trend is reversed upon crossing the threshold of 0.9 equivalence ratio and for stoichiometric and rich conditions (Φ = 1.0, 1.1). At Φ = 0.8, NO is more uniformly distributed along the flame front although a slight decrease in its mass fraction can be observed at the cusp pointing towards the burnt products, i.e. concave. Please note that, for better and more immediate comparison, while at the higher equivalence ratios (Φ = 0.9, 1.0, 1.1) it was possible to obtain nearly identical wrinkled flame fronts (due to similar flame velocities), at the lower equivalence ratios (Φ = 0.3, 0.45, 0.8) the same convenient visualization was not possible because of largely different temporal evolution of the flame fronts (due to different flame velocities). Figure 3 quantifies the local change in OH and NO mass fractions and temperature downstream of the flame reaction layer. In the course of the present analysis, we define the reaction layer for values of the progress variable between $0.6 \leq C \leq 0.8$ (corresponding to the vicinity of the peak heat release rate) while higher values $C > 0.8$ are defined as "downstream of the flame reaction layer". The NO mass fraction and other properties are analyzed along lines normal to the flame reaction layer defined using isolines corresponding to peak heat release rate (this methodology is described in more detail in Section 3.2). In Fig. 3 the absolute maximum and minimum values of the NO mass fraction, for each value of the global equivalence ratio, is selected over the simulation time. These are related to the average increase, or decrease, in NO mass fraction downstream of the reaction layer for concave and convex portions of the flame front, respectively. For the chosen values of the NO mass fraction, OH and temperature's corresponding values are selected and related to their mean. The observed local changes in OH and NO mass fractions are more pronounced at very lean conditions, with 70% and 40% respectively, and at rich conditions with changes up to 50% and 30% respectively, whereas close to stoichiometry (Φ = 0.8 and Φ = 0.9), the local changes in OH and NO mass fractions are significantly lower. The observed changes in the local temperature are, however, smaller with a maximum variation of 7% and do not show the same distinctive trend as NO and OH.

The portions of the flame front that are characterized by higher NO concentrations are always spatially correlated with regions of

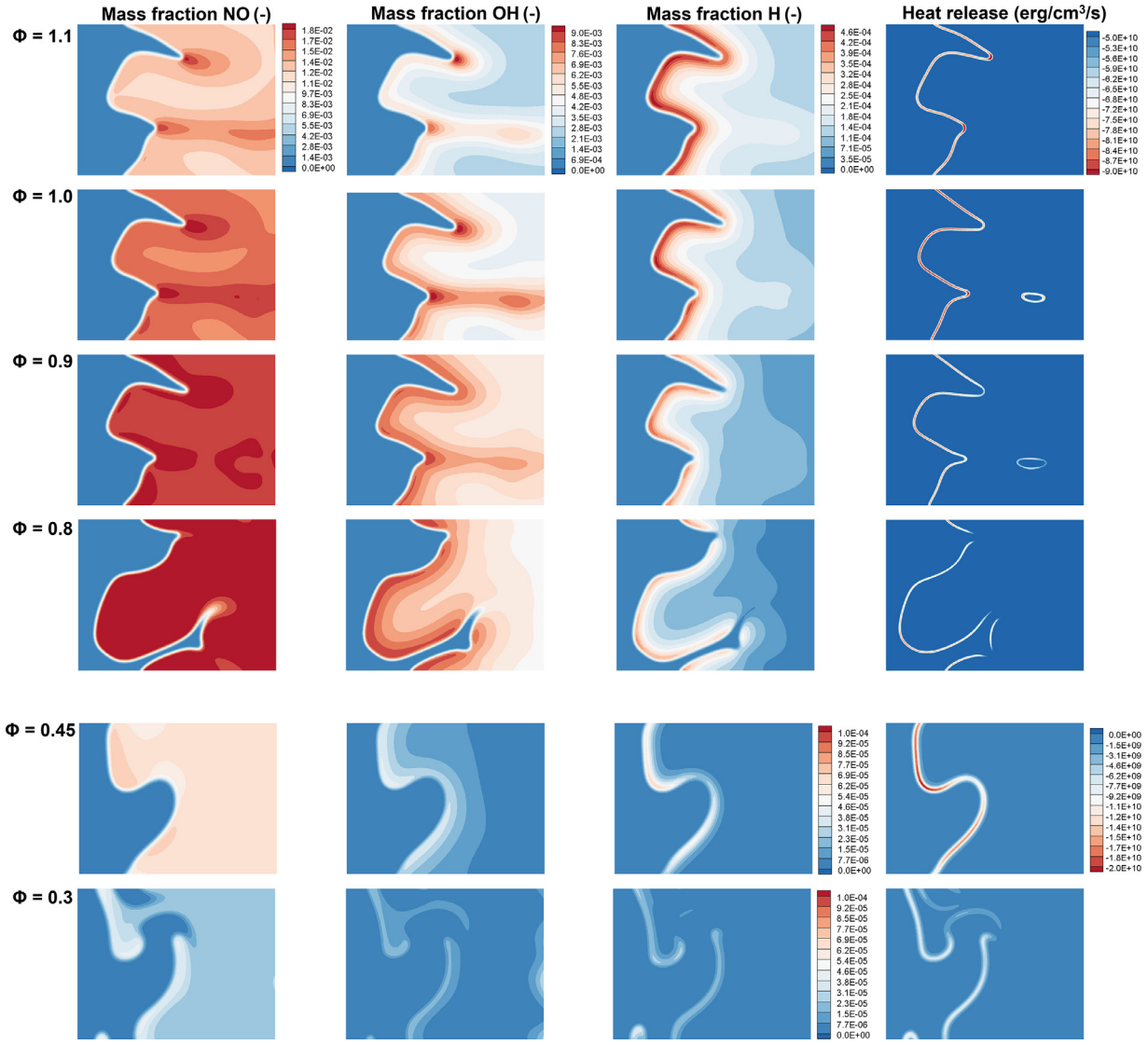

Fig. 2. Premixed wrinkled flame fronts at 1 ms simulation time for all equivalence ratios studied. Contours of NO, OH and H mass fractions are shown from left to right.

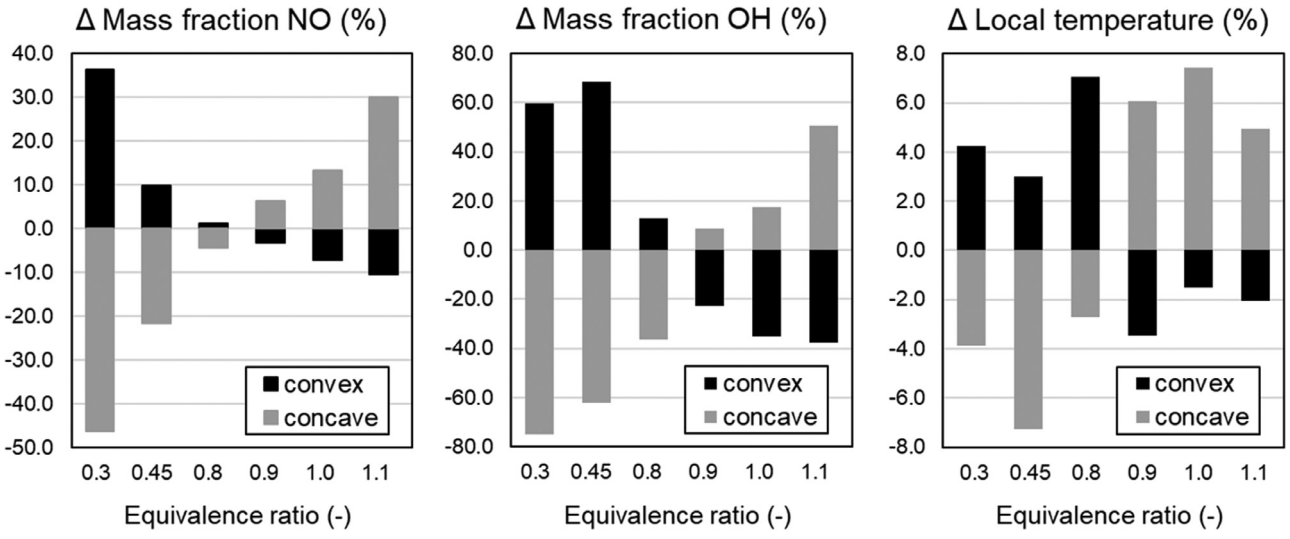

Fig. 3. Relative change in OH and NO mass fractions and local temperature downstream of the wrinkled reaction layer in concave- and convex-shaped portions of the flame front.

Table 1
Laminar flame properties for the fuel blends investigated in the DNS.

Equivalence ratio (-)	0.3	0.45	0.8	0.9	1.0	1.1
Laminar flame speed (cm/s)	30.9	87.0	208.2	233.3	250.6	258.5
Laminar flame thickness (mm)	1.545	0.857	1.163	1.183	1.185	0.941
Laminar flame time (ms)	5.0	0.98	0.56	0.50	0.47	0.36
Inner layer temperature (K)	1358.9	1484.3	1691.8	1727.3	1750.9	1757.8
Temperature at maximal radical production (K)	1417.8	1603.3	1915.5	1976.3	2023.3	2053.4
Adiabatic flame temperature (K)	1492.2	1772.6	2254.6	2347.2	2405.0	2405.4

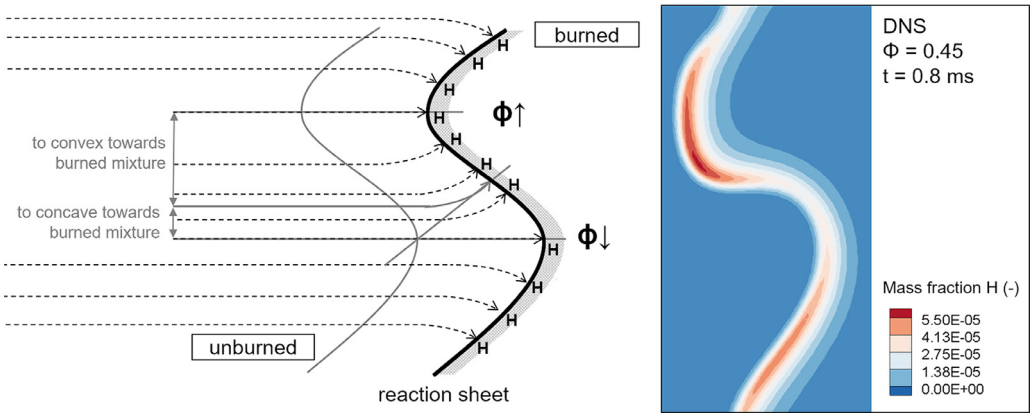

Fig. 4. Sketch of the streamlines pattern as they approach the flame front according to [29] and the resulting change in local equivalence ratio (DNS data is shown for comparison). Black dashed lines represent the flow streamlines.

increased OH concentrations. These regions are accompanied, at lean conditions, by local enhancement of the heat release rate in convex-shaped portions of the flame front (see Appendix) and their spatial pattern. This observation in the present study is consistent with earlier observations found in the open literature [17]. At the higher equivalence ratios considered here, on the other hand, high NO concentrations are present at the concave-shaped portions of the flame front and correlated with low values of the heat release rate (compared to elsewhere along the flame front). This observation seems to suggest that NO formation patterns in these $NH_3/H_2/N_2$-air flames are not necessarily correlated with high values of the heat release rate and, consequently, of the local temperature (due to the Zel'dovich mechanism).

The occurrence of high values of the H radical concentration in the convex-shaped portions of the flame front is related to the fast diffusion of hydrogen species (H_2 and H). While molecular hydrogen (H_2) migrates faster than the other species from the fresh reactants' side towards the reaction layer [29], atomic hydrogen (H radical) is produced in larger quantities therein. Note that H_2, diffusing towards the reaction zone, concentrate in convex portions of the flame front while they diffuse away from it in concave portions ("open tip" phenomenon), this is qualitatively illustrated in the sketch of Fig. 4 [29]. The Soret effect, i.e. thermal diffusion, leads to additional H_2 diffusion towards relatively hotter regions increasing local enrichment or fall-off in the equivalence ratio, which we defined using the elemental mass fractions of hydrogen Z_H and oxygen Z_O related to their stoichiometric (subscript st) ratio in the unreacted (subscript u) mixture:

$$\Phi_{local} = \frac{Z_H/Z_O}{(Z_{H,u}/Z_{O,u})_{st}} \tag{2}$$

and

$$Z_i = \sum_{j=1}^{S} \mu_{ij} Y_j \tag{3}$$

where, i is the considered element, S the total number of species, j the species and μ_{ij} the mass proportion of i in j. Consequently,

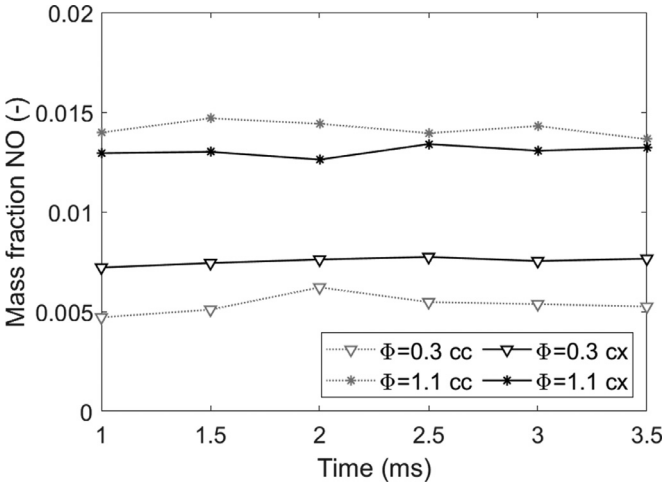

Fig. 5. Temporal evolution of the NO mass fraction in concave and convex shaped portions of the flame front for the richest ($\Phi = 1.1$) and the leanest ($\Phi = 0.3$) analyzed mixture.

the local laminar flame speeds also increases or decreases, depending on the local equivalence ratio, resulting in differential acceleration of different portions of the flame front that, in turn, increases flame wrinkling and the generation of additional flame surface. The impact of thermal diffusion on the formation of NO is quantified in Section 3.6.

The observed NO formation pattern is established after 1 ms of simulation time and remains unchanged over the transient simulation period. The reaction front spatial motion and its curvature do not reach steady-state since the flame is continuously wrinkled due to the vorticity present in the approaching reactants' flow and also because of the resulting local variations in the acceleration of the reaction front itself. However, Figure 5 clearly indicates that NO mass fraction values tend to a statistically steady value. The comparison between the 2D DNS data and the 1D steady-state simula-

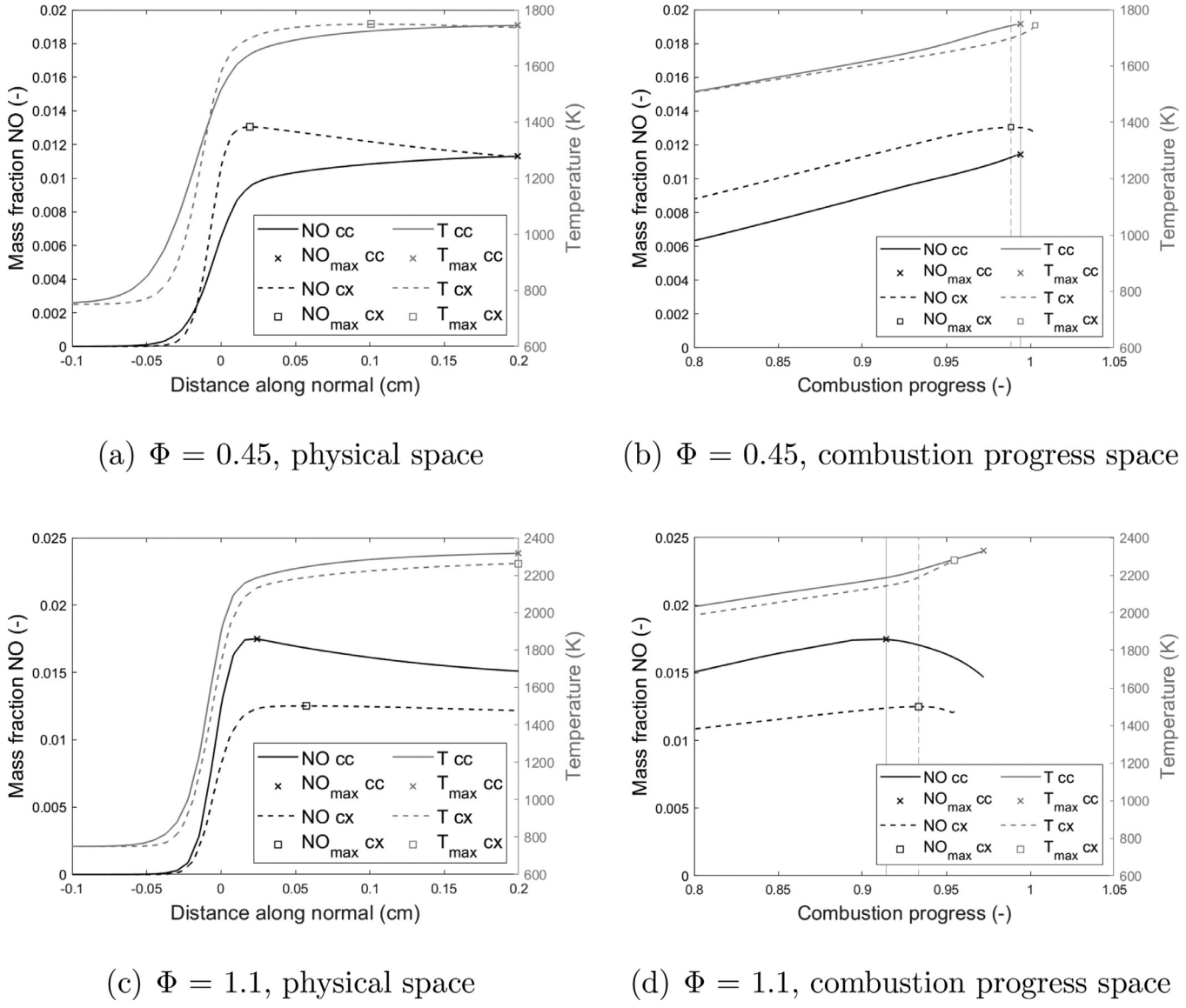

(a) $\Phi = 0.45$, physical space

(b) $\Phi = 0.45$, combustion progress space

(c) $\Phi = 1.1$, physical space

(d) $\Phi = 1.1$, combustion progress space

Fig. 6. Exemplary spatial evolution of NO mass fraction and temperature along lines normal to the reaction layer in convex and concave portions of the flame front. Symbols mark the maximum values.

tions, discussed in Section 3.3 and indicating similar NO mass fraction values, confirms that the NO mass fractions can be assumed to be statistically steady-state.

3.2. Quantitative analysis of the flame front

In order to understand the inter-dependency between fast hydrogen species diffusion, local concentrations of radical species along the wrinkled flame front and, ultimately, the production rates of NO, we conduct a detailed, quantitative analysis of the chemical reaction kinetics for opportunely selected representative portions of the wrinkled flame front. For this analysis, temperature, concentrations and reaction rates for all species are extracted along lines perpendicular to the flame front, in correspondence of concave "cusps" towards the products and convex "bulges" towards the reactants, for all equivalence ratios considered. In order to meaningfully compare the quantities extracted from the DNS database, the line-data is normalized with respect to the flame front using the maximum rate of O_2 consumption, as proposed in [16]. The selected values of species concentrations and temperature are sampled immediately downstream of the reaction layer (as defined earlier). This behavior is illustrated in Fig. 6.

In order to identify any eventual major dependency of NO mass fraction on the flame characteristics, first order correlation coefficients (R values) are calculated over several time steps (1–3.5 ms in 0.5 ms steps) for all equivalence ratios considered. A linear weighted regression is calculated where the weighting is implemented according to the mean value of the NO mass fraction. The curvature K is calculated from isolines extracted at $C = 0.6$ marking the upstream limit of the reaction layer in our definition. Second-order polynomials are fitted to the extracted isolines in order to obtain their parametric representation expressed as L(x)=(a(x),b(x)). Conveniently, this polynomial representation allows the calculation of the flame front curvature using first and second derivatives:

$$K(x) = \frac{a'(x)b''(x) - b'(x)a''(x)}{(a'^2(x) + b'^2(x))^{(3/2)}} \tag{4}$$

For a more convenient comparison, the instantaneous values are normalized by the maximum value of the curvature over all time

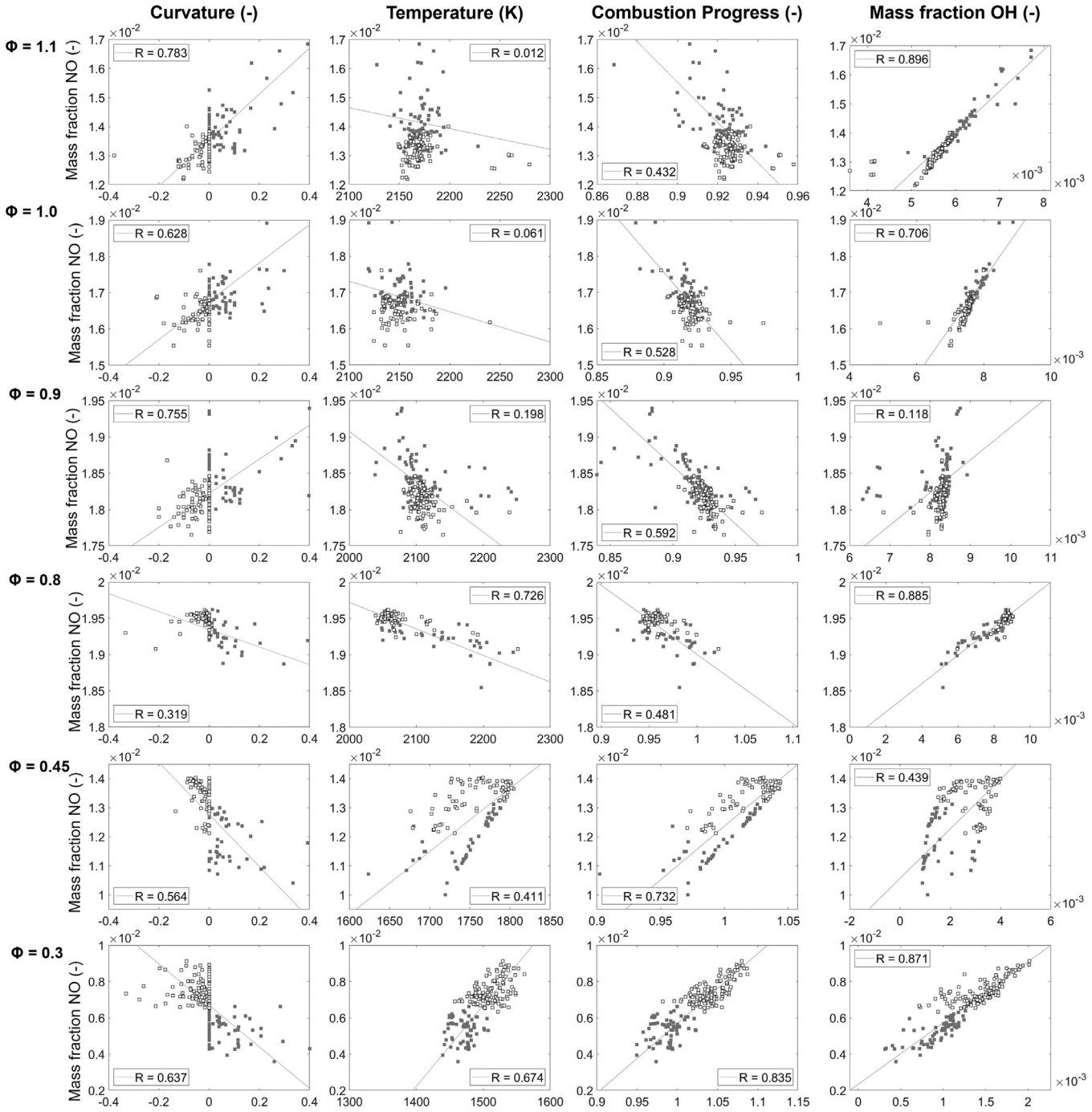

Fig. 7. Local maxima in NO mass fraction, for convex (black, open symbols) and concave (gray, filled symbols) portions of the flame front, versus corresponding normalized flame front curvature, local temperatures and OH mass fraction.

steps considered. Here, the normalized flame curvature k, defines convex regions by $k < 0$ and concave ones by $k > 0$.

The correlations shown in Figs. 7 and 8 illustrate the relationship between NO mass fraction and selected flame characteristics, such as local curvature, local temperatures, combustion progress and OH, O_2, N_2 mass fractions. Their inspection suggests that NO mass fraction correlates well with the local equivalence ratio and the corresponding oxygen level. These correlations gain weight towards lean and rich conditions where the increase and decrease of NO and OH formation is most pronounced (compare Fig. 3). For all global equivalence ratios, a correlation with the normalized curvature is found. Nevertheless, this correlation is weaker compared to the one associated to local equivalence ratio. Due to the disparities in *global* equivalence ratio (indicated in the figure), however, the unsteady flame surfaces evolve differently in the DNS calculations and, ultimately, this results in flame shapes and a reaction front curvature that may not be directly comparable at homologous simulation times (Fig. 2). The present methodology takes into account the NO mass fraction values but do not directly consider the size of the area upon which NO is distributed. This issue is further discussed in Section 3.6, and it is supported by Figs. A1 and A2 in the Appendix (with increasing curvature the affected portion of the post flame becomes larger). In general, the present results suggest that trends in local NO formation largely depend on the

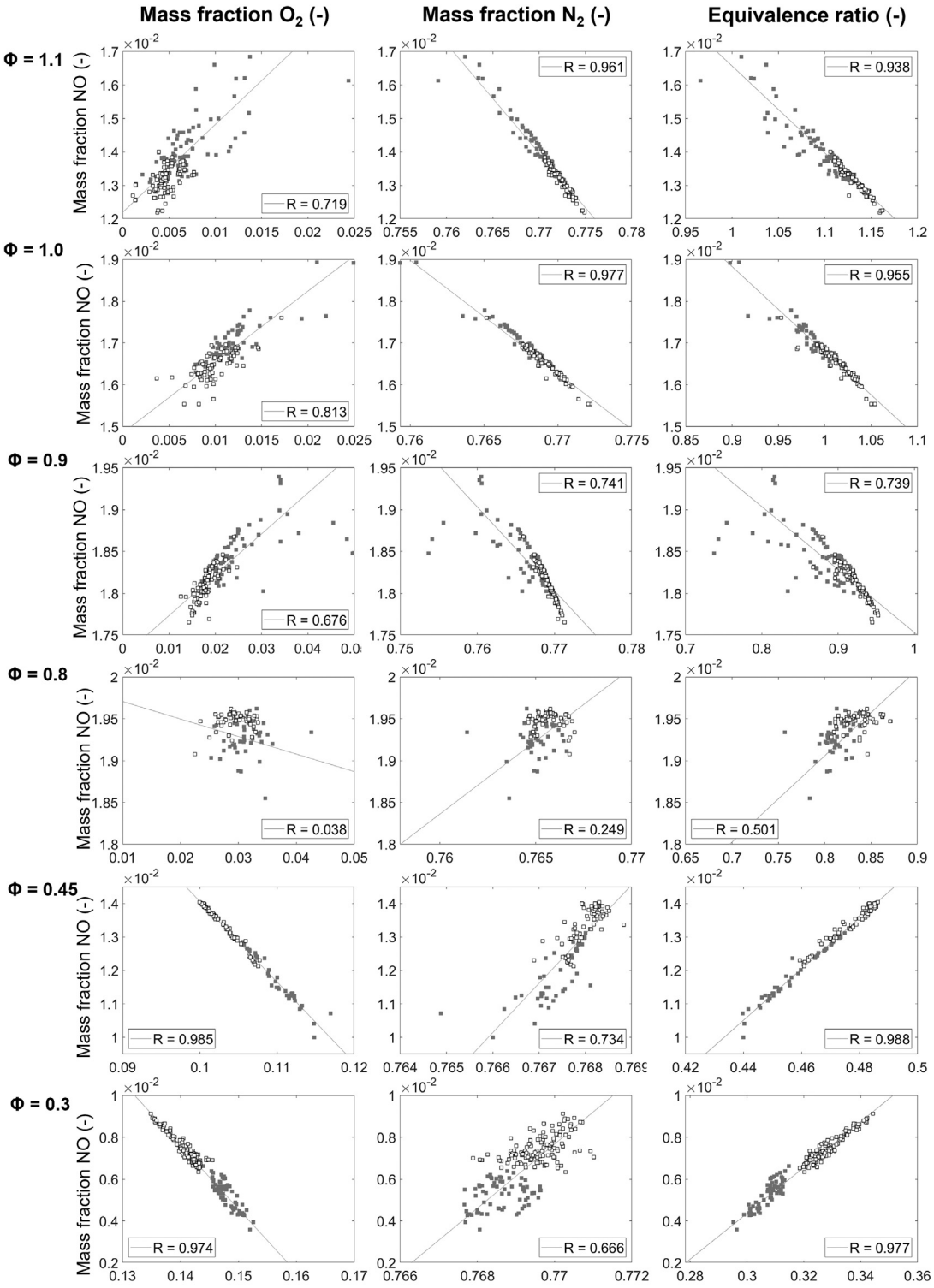

Fig. 8. Local maxima in NO mass fraction, for convex (black, open symbols) and concave (gray, filled symbols) portions of the flame front, versus O_2, N_2 mass fractions and local equivalence ratio.

sign of the flame curvature but not necessarily (to a first order approximation) on its strength.

The leaner the global mixture, the stronger NO correlates with the local temperature and combustion progress. With decreasing global equivalence ratio, the combustion progress at which the local maximum and minimum NO mass fraction are located increases. For very lean conditions ($\Phi \leq 0.45$) superadiabatic conditions are observed. At moderately lean conditions ($\Phi = 0.8$ and $\Phi = 0.45$), NO formation is enhanced in convex shaped portions of the flame front while the local temperature is comparable to the one observed in concave ones. At rich conditions ($\Phi \geq 0.9$), conversely, the temperatures observed in concave and convex portions of the flame front are similar but NO formation is larger in concave ones. For increasingly lean conditions, the temperature impact in-

creases, so that at $\Phi = 0.3$, the higher NO values are correlated to the higher temperatures.

The reason for this distinct trend is twofold. Firstly, the characteristic spatial pattern of maximum NO concentration differs between rich and lean conditions. In regions with increased OH activity, local peaks in NO concentration are observed to be very close to the reaction zone of the flame while the temperature still increases further downstream towards the combustion products and the post-flame zone (Fig. 6). Conversely, in regions with reduced OH activity, local peaks in NO concentration are found downstream of the reaction zone and are co-located with the maximum temperature. This trend is more distinctive at lean conditions, for rich conditions ($\Phi > 0.9$), peak NO mass fractions occur shortly after the flame reaction layer and it remains at this level further downstream. Secondly, but not least importantly, the NO chemistry seems to be affected by preferential diffusion of H_2 and by the resulting local radical pool, available oxygen O_2 and the local change in equivalence ratio, as these are closely correlated. The previous statement will be clarified in the discussion about the role of thermal diffusion (the Soret effect) presented in Section 3.6.

3.3. Role of the local equivalence ratio

It has been discussed earlier how the preferential diffusion characteristics of hydrogen species (H radical and molecular hydrogen) lead to changes in the local equivalence ratio of the reacting mixture [29]. The *local* change in equivalence ratio is shown in Fig. 9 and along lines extracted perpendicularly to the flame front in Fig. 10, for all global equivalence ratios considered in this work. Note Fig. 10 is split in two plots for improved clarity. In all convex-shaped portions of the flame front (solid line) the local equivalence ratio, after an initial reduction, increases beyond its initial (global) value within the reaction zone, while, for the concave-shaped portions of the flame front, it decreases to a value below its initial (global) value. In these concave-shaped portions of the flame front the local equivalence ratio reaches again the global value further downstream of the reaction zone (except for $\Phi = 1.1$, where the local value of the equivalence ratio always remain below the global value). For increasingly high global equivalence ratios, the absolute change in equivalence ratio increases from $\Delta_{\Phi=0.3} = 0.02$ to $\Delta_{\Phi=1.1} = 0.15$ for convex-shaped portions of the flame front, with reductions of the same order in concave-shaped ones. However, the relative change in equivalence ratio is similar, over the whole range investigated and varies between 5% and 15%, which is smaller than the increase/decrease in OH and NO mass fractions (Fig. 3). Figure 10 only shows a portion of the flame-normal, one-dimensional region very close to the flame front. All local equivalence ratios converge to the initial global equivalence ratio further downstream (Fig. 9). Local differences in the supply of fuel to the reaction zone is thus affecting the combustion kinetics of this region of the flame, including the NO production and consumption chemistry. The dependency on local equivalence ratio can be studied more conveniently by using one-dimensional (1-D) premixed flames (here: freely propagating flames obtained by the module available within LOGEresearch 1.10 [30]) to analyse the local chemistry for comparison with the 2-D DNS data. The local equivalence ratios after the flame front, at $x = 0.025$ cm, are extracted and imposed into 1-D premixed flames calculations. The equivalence ratio obtained from the 2-D DNS data is enforced in the 1-D calculations by mixing the unreacted fuel blend with air. This means that no other species are included except the stable species, in order to isolate and investigate the impact of the local equivalence ratio. In these 1-D simulations, the trends in NO formation predicted by the 2-D DNS calculations between the convex versus the concave regions of the flame front are replicated, as illustrated in Fig. 11. The present analysis suggests indeed that local equivalence ratio variations due to flame curvature play a significant role on the formation of NO in ammonia/hydrogen combustion.

Note that other recently updated chemical kinetic schemes available in the open literature [31–33] have been tested and predict similar trends, thereby confirming that the present observations are independent of the specific reaction scheme adopted in the DNS calculations, although absolute values of NO differ somewhat between the different kinetic schemes (Fig. 12).

3.4. Analysis of the NO chemistry

In order to understand how NO formation is affected by local equivalence ratio changes that are caused, in turn, by wrinkling of the flame front, the mass fraction of selected species is first plotted against the mixture's equivalence ratio and presented in Fig. 13 based on data from 1-D numerical simulations of laminar premixed flames. At globally lean conditions, an increase in equivalence ratio enhances the production of NO due to the availability of additional fuel and the resulting increase in the adiabatic flame temperature. This trend is reversed at $\Phi = 0.8$ where, upon further increase of the equivalence ratio, a decrease in NO is observed, due to the increasing scarcity of O_2. The trend clearly illustrated by the analysis of 1-D data well reflects the homologous peak in mass fraction NO at a global $\Phi = 0.8$ observed from the 2-D DNS data. Note that the peak in mass fraction NO at $\Phi(NO_{\max}) = 0.8$ is spatially closer to the peaks in mass fraction O and OH rather than to the peak in adiabatic flame temperature which is, for this mixture, at $\Phi(T_{ad,max}) = 1.06$. In the 2-D wrinkled flames, convex-shaped portions of the flame front protruding into the reactants are subject to local enrichment, thus whether the global equivalence ratio is smaller or higher than $\Phi = 0.8$ will determine an increase or decrease of NO concentration. This finding is supported by the 1-D analysis and the comparison of the 1-D with the 2-D DNS data in Fig. 13(b). Furthermore, since the NO mass fraction peaks at $\Phi = 0.8$, small changes in the local equivalence ratio, either towards lean or rich conditions, lead to a decrease in NO formation. Ultimately, this implies a somewhat weaker dependency on the local equivalence ratio but the NO sensitivity to local temperature is increased, as indicated by the first order correlations (Figs. 7 and 8). Note that preferential diffusion of H_2 leads not only to a change in local equivalence ratio but also in local hydrogen/ammonia ratio as well as depletion of O_2, as discussed below.

A reaction sensitivity analysis towards NO formation is carried out in order to identify the nature of the driving NO chemistry. Note that, in the following, reactions are numbered according to the original mechanism for consistency (all elementary reactions discussed here are printed in Table 2). At lean conditions NO production is highly sensitive to fuel NO pathways such as R32, R35 and R44 in [13], whereas thermal NO production (R50, R58, R59) becomes more dominant under rich conditions as the adiabatic flame temperature increases. This aligns with the strong correlation of NO to mass fraction N_2 at rich conditions, with reference to Fig. 8. Figure 14 shows the characteristic of the reaction system: two competing pathways of NH_3 consumption through the formation of NH_2 leading, in turn, to competing routes for N_2 and NO formation. At rich conditions, the N_2 formation pathway via NH and N is dominant, while in leaner mixtures, the NO formation via HNO gets increasingly important. This competition of the pathways is also present in the other investigated mechanisms presented in Fig. 12. NO is additionally formed to a certain amount by the oxidation of NH and N and the pathway via R39 is present under lean conditions only. The important role of NH_2 decomposition and NO formation via HNO is also observed in [9] for many different reaction mechanisms, whereas the authors discuss pathways for different temperatures and equivalence ratios.

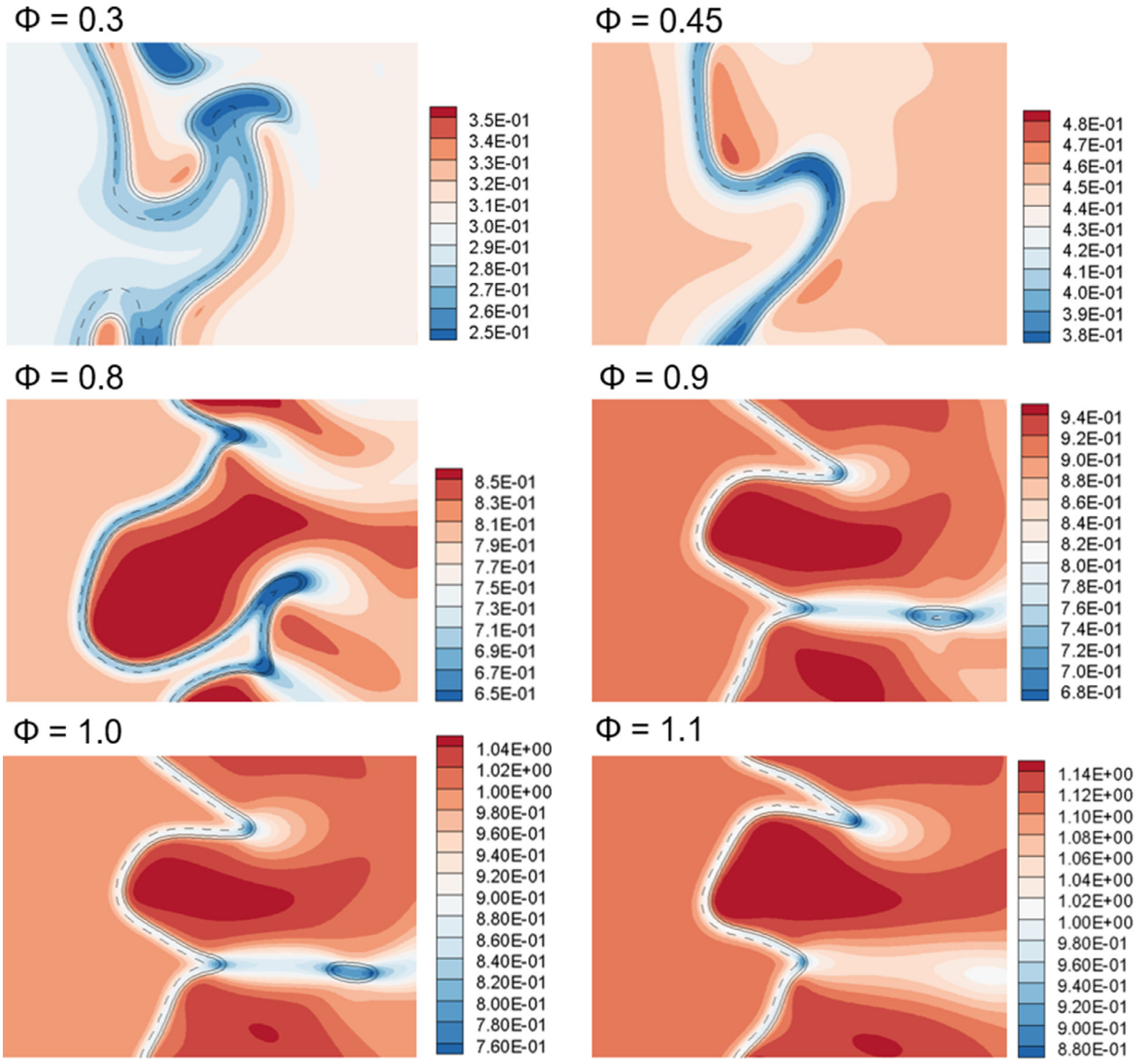

Fig. 9. Spatial variation in the reacting mixtures' local equivalence ratio. Dashed lines denote the preheat layer (C = 0.1), solid black lines the combustion zone (0.6 < C < 0.8).

Table 2
Selected reactions, from the mechanism by Jiang et al. [13], that affect directly or indirectly the NO chemistry.

Reaction number	Reaction
R1	H_2+O = OH+H
R2	H+O_2 = OH+O
R9	H+O_2 = HO_2
R32	NH_2+N = N_2+H+H
R33	NH_2+O = HNO+H
R35	NH_2+NO = N_2+H_2O
R39	NH+O = NO+H
R44	NH+NO = N_2+OH
R50	N_2+O = N+NO
R52	HNO (+M) = NO+H (+M)
R56	HNO+OH = NO+H_2O
R58	N+O_2 = NO+O
R59	N+OH = NO+H

3.4.1. Lean conditions

Lean conditions (Φ = 0.45) favor the decomposition pathway of NH_2 via HNO. Moreover, H_2 diffusing into the convex-shaped flame portion will lead to an increased production of H, O and OH radicals via the highly sensitive reactions R1 and R2. This radical pool enhances the pathway via HNO further (R33) and lead to an increase in reaction rate of reaction R56. Increased O_2 consumption, via reactions R1 and R9, drives the equilibrium of R52 towards higher production of NO. The shift is visible in Fig. 15, where reaction R52 is exothermic in convex-shaped portions of the flame front, while it is endothermic in concave ones. The increased O_2 consumption in convex-shaped sections of the flame front results in the clearly distinguishable region of lower mass fraction O_2 shown in Fig. 16 and leading to strong correlations with the local mass fraction O_2, in reference to Fig. 8. Overall, the increased equivalence ratio, the increased H_2 concentration and the availability of O_2 cause higher NO formation in convex portions of the flame front compared to concave ones.

The impact on NO formation of the available radical pool is also discussed by Okafor et al. [12]. The authors, in their study on a low-NO_x ammonia combustor for a micro gas turbine, found a correlation between OH and local equivalence ratio profiles in 3-D Large Eddy Simulation (LES). They concluded that controlling the global equivalence ratio (through staging) may provide some level of control on O, H and OH radicals availability and consequently the NO_x emission.

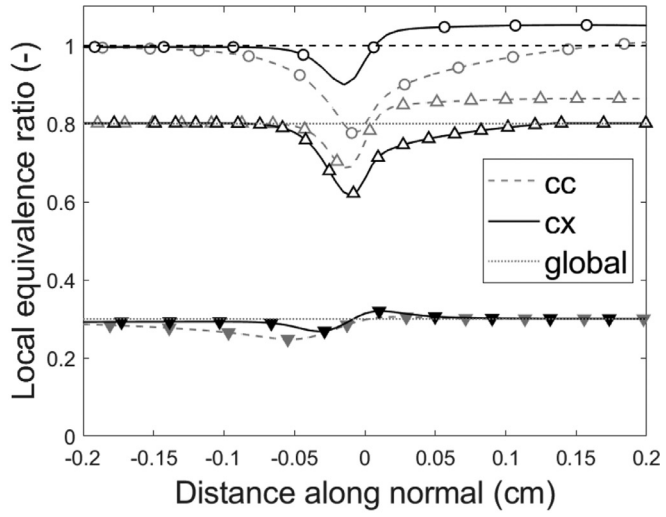

(a) $\Phi = 1.0$, $\Phi = 0.8$ and $\Phi = 0.3$

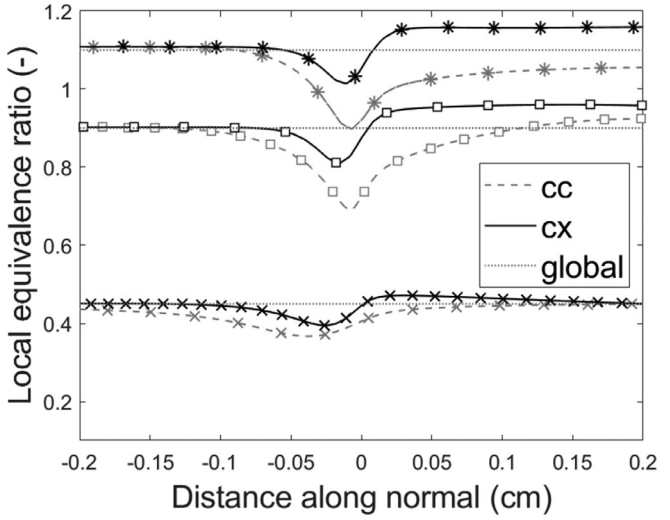

(b) $\Phi = 1.1$, $\Phi = 0.9$ and $\Phi = 0.45$

Fig. 10. Spatial variation in the reacting mixtures' local equivalence ratio along lines extracted perpendicularly to the flame front for the different global equivalence ratios considered in this study.

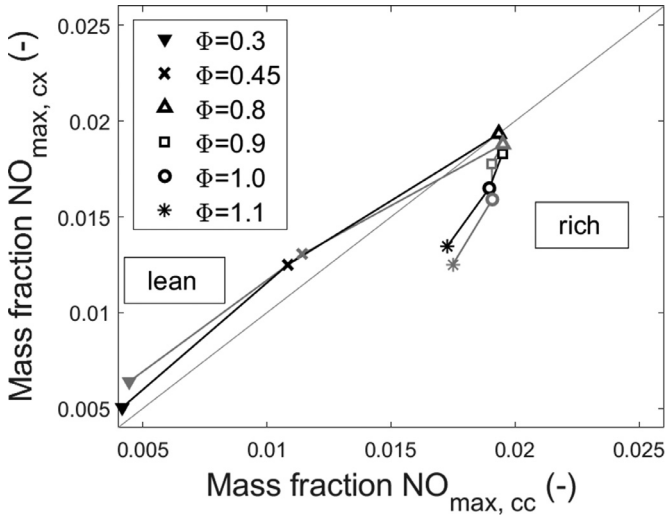

Fig. 11. Maximum NO mass fraction in concave versus convex regions. Comparison between the 2-D DNS data and 1-D laminar flame predictions. Gray symbols: DNS data as in Fig. 7. Black symbols: predicted trends using 1-D laminar premixed flames.

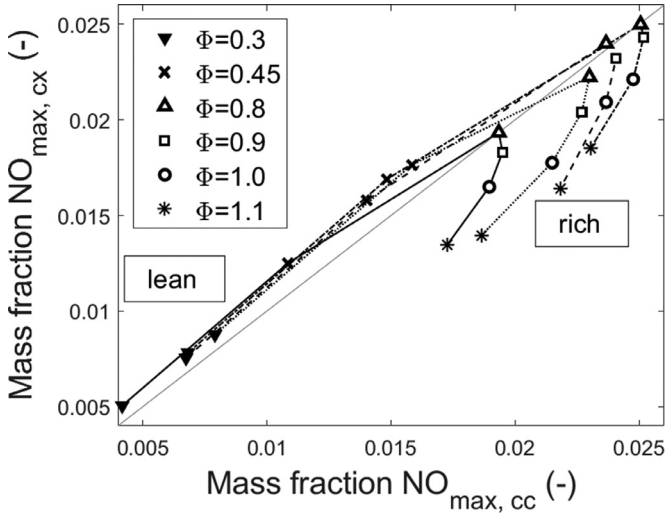

Fig. 12. Maximum NO mass fraction in concave versus convex regions. Comparison between different chemical kinetics mechanisms. Solid line: Jiang et al. [13], used in the present DNS calculations. Dashed line: Shrestha et al. [31]. Dotted line: Otomo et al. [32]. Dash-dotted line: Glarborg et al. [33].

3.4.2. Role of the hydrogen/ammonia ratio

The preferential diffusion of H_2 affects the local equivalence ratio, but also the local composition of the $NH_3/H_2/N_2$ fuel blend since H_2 concentration is increased or decreased. In order to understand how important is the impact of the change in the hydrogen/ammonia ratio in the fuel blend on the reaction system, three different mixtures are compared. The 2-D DNS simulations are carried out for a fuel blend of 40% NH_3, 45% H_2 and 15% N_2 by volume. In the mentioned fuel blend, the hydrogen/ammonia ratio (on mass basis) is H_2/NH_3 = 11.6%/88.4%. This ratio is compared to the homologous ratio observed at the location of maximum NO concentrations (Fig. 6) for convex and concave portions of the flame front. For example, at $\Phi = 1.1$, molecular diffusion changes this ratio in concave portions of the flame front to H_2/NH_3 = 9.6%/90.4% and in convex ones to H_2/NH_3 = 12.7%/87.3%, relatively to the unburned mixture. For each of the H_2/NH_3 ratios listed, a flow analysis is carried out and results are shown in Fig. 17. The consumption percentages show that the increase of H_2 in respect to NH_3 leads to an additional enhancement of the dominant pathway of NH_2 consumption via NH and the direct formation of N_2. The further decomposition of NH to N is, in the case of concave-shaped portions of the flame, with a decrease of H_2 in the H_2/NH_3 ratio, limited to 58.4% consumption, whereas with higher local H_2 amount it is increased to almost 69%. The decrease of H_2 in the local fuel blend further leads to an augmentation of the NO formation via HNO. However, the further conversion of NO to N_2 is limited, as consequence more of the formed NO remains. Together with the increase in OH radical concentration and higher heat release rate in the concave-shaped flame fronts, as previously discussed, more NO is formed. The trend observed in the 1-D simulations agrees well with the 2-D DNS results where areas with lower H_2 concentration have higher NO levels (Fig. 16).

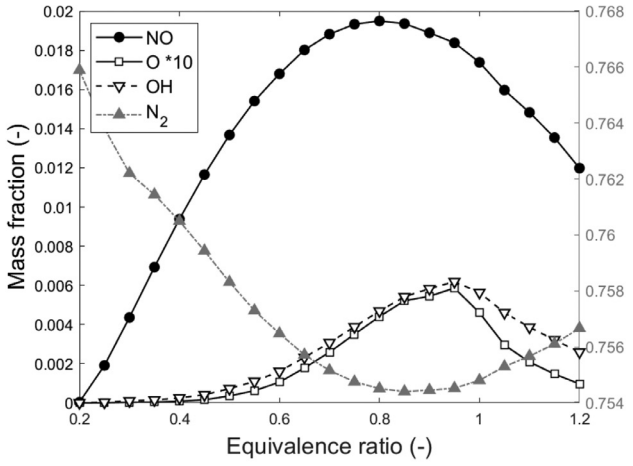

(a) 1-D premixed laminar flames

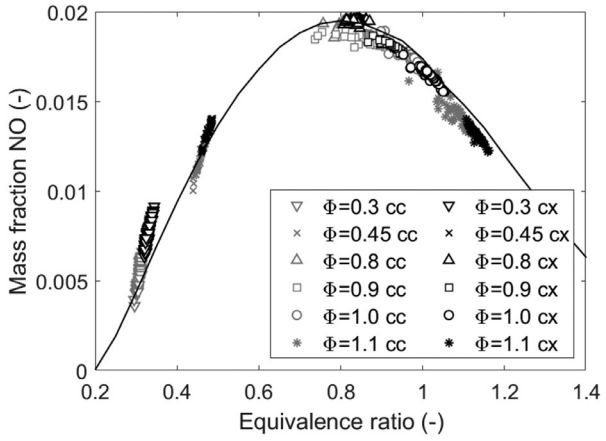

(b) Symbols: 2-D DNS flames data, solid line: 1-D flames data

Fig. 13. Mass fractions of selected species over equivalence ratio in 1-D premixed laminar flames (N_2 goes with right y-axis) and comparison to the DNS results.

3.4.3. Depletion of oxygen

Another effect of the fast H_2 diffusion into the convex portions of the flame front is the depletion of O_2. By analysing O_2 concentration profiles along the lines extracted normally to the flame front, it is found that H_2 diffusion into the convex-shaped flame leads to depletion of the oxidizer and a significant decrease in local O_2 concentration. Whereas O_2 depletion does not play a key rate-limiting role at the leaner conditions investigated due to the considerable surplus of O_2 that is present, it definitively drives the local equivalence ratio further towards stoichiometry for $\Phi = 0.9$ and towards richer conditions for $\Phi > 1.0$ and, consequently, leads to lower production of NO. As discussed earlier, the turning point for this equivalence ratio scaling of the NO formation is at $\Phi = 0.8$ (Fig. 13). This is where the highest NO formation and the smallest difference between concave and convex-shaped portions of the flame are found.

3.5. Impact of the specific fuel blend

A second fuel blend, nominally a result of lower degree of ammonia cracking, is analyzed in order to understand the sensitivity

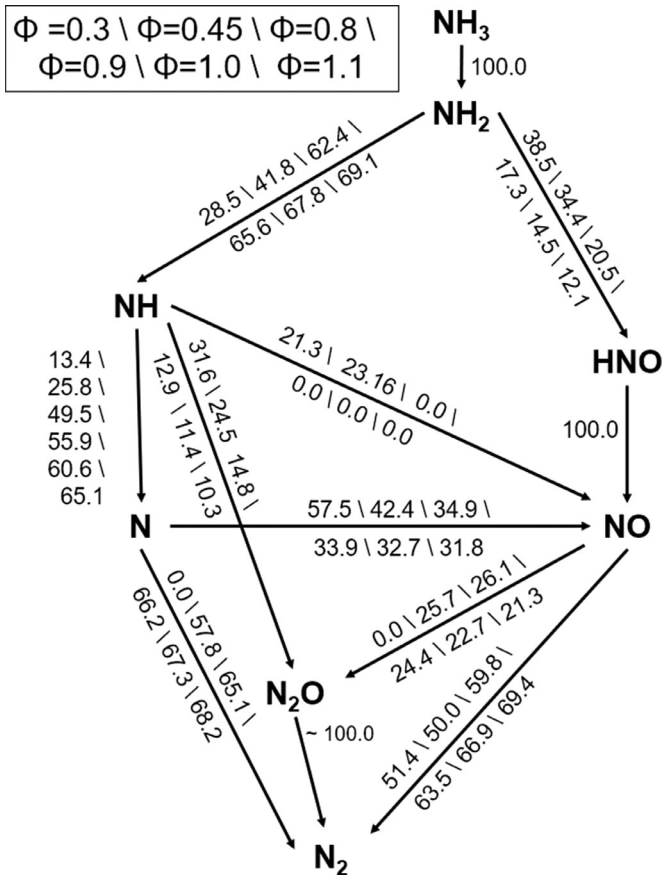

Fig. 14. Flow analysis of the main fuel nitrogen pathways. Percentages give the consumption fluxes at different equivalence ratios.

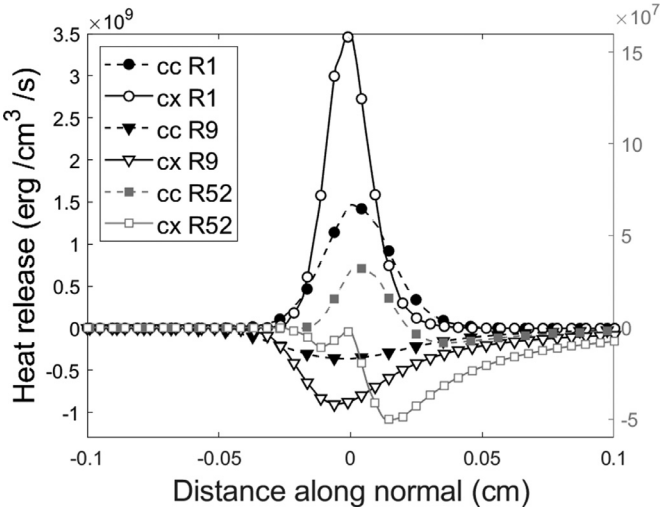

Fig. 15. Heat release rate for reactions R1, R9 and R52 along lines extracted perpendicularly to the flame front in concave and convex flame portions at $\Phi = 0.45$. Labels for R52 on the right y-axis.

of the NO formation process to the fuel blend. This second fuel blend is set to 21% H_2, 72% NH_3 and 7% N_2 by volume and its combustion in air simulated within a 2-D configuration that is otherwise identical to that used for the first blend, as previously discussed. Fuel lean ($\Phi = 0.45$) and fuel rich ($\Phi = 1.1$) conditions are investigated.

Inspection of Fig. 18 shows that for this second fuel blend the characteristic spatial pattern of NO concentration is similar to the

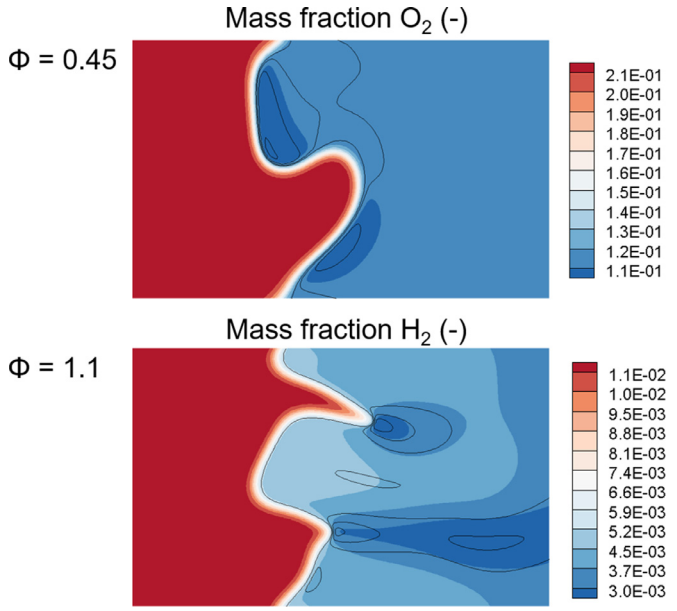

Fig. 16. Contours of O_2 mass fraction at 1 ms for Φ=0.45 and H_2 mass fraction at 1 ms for Φ=1.1. Black lines indicate the NO islands in Fig. 2.

one indicated previously for the first fuel blend: at rich conditions, NO formation is enforced in concave shaped portions of the flame and, at lean conditions, in the convex ones. Overall, the peak NO mass fractions are lower compared to the first fuel blend with a maximum mass fraction of Y_{NOmax}(blend 2) = 0.013 (Y_{NOmax}(blend 1) = 0.02). The location of this maximum is shifted to Φ = 0.85. The regression lines show that, for blend 2, the impact of the flame front curvature and local temperature increase compared to blend 1, however the strong dependency on the local equivalence ratio remains (Fig. 19). The increased sensitivity to curvature and temperature can be related to the lower hydrogen content, where hydrogen diffusion becomes the limiting factor. It affects the local equivalence ratio, depending on the local geometrical features of the flame, as well as the local temperatures (see Fig. 7). Ultimately, the lowered hydrogen content in the fuel blend leads to lower NO formation, even though local temperatures are higher and a nitrogen-containing fuel is still present. This finding confirms the dominant role of preferential diffusion of H_2 on the local equivalence ratio and therewith OH and NO formation.

3.6. Impact of thermal diffusion (Soret effect)

The fluid temperature is not only impacting the reaction rates of the chemical kinetics, but it also represents the main driving force behind thermal diffusion (Soret effect). In order to quantify the impact of the Soret effect on the observed NO formation patterns, otherwise identical 2-D DNS calculations are repeated without accounting for thermal diffusion within the mixture-averaged diffusion model (it is included in all calculations considered up to this point). Figure 20 illustrates, for an equivalence ratio Φ = 0.45, a comparison of the NO mass fraction spatial distribution throughout the computational domain from calculations performed with (top) and without (bottom) taking into account thermal diffusion. Minor differences in the curvature of the flame front are visible, these are caused by differences in local equivalence ratio (impacted by thermal diffusion) that, in turn, affect local flame speed. As the simulations advances in time these curvature differences become more evident. Here, a relatively early time (t = 1.1 ms) is chosen in order to more conveniently compare homologous features of the flame front: in the absence of thermal diffusion the regions of high NO mass fraction appear smaller.

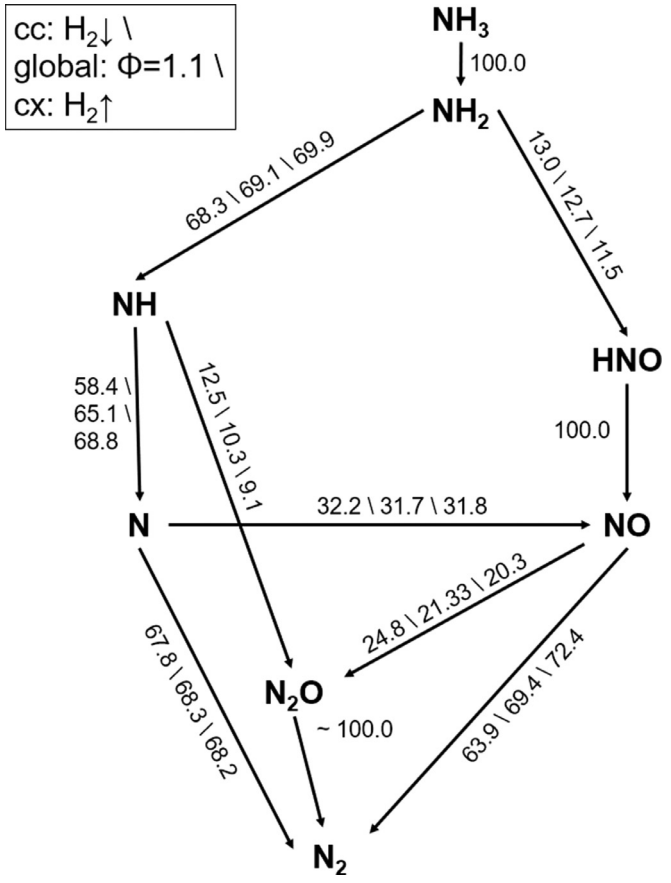

Fig. 17. Flow analysis of the main fuel nitrogen pathways. Percentages indicate the consumption of the initial fuel species ratio (H_2/NH_3 = 11.6%/88.4%) and their ratio in concave (H_2/NH_3 = 9.6%/90.4%) and convex (H_2/NH_3 = 12.7%/87.3%) portions of the flame front for Φ = 1.1.

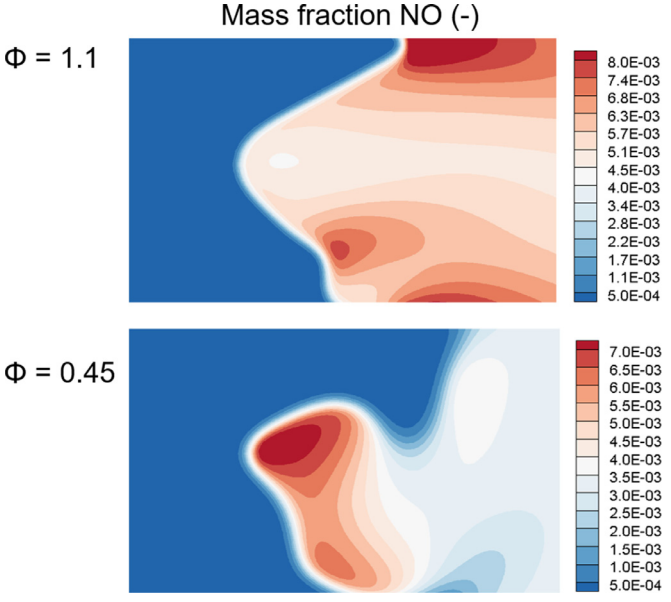

Fig. 18. Contours of NO mass fractions at 4 ms for Φ = 0.45 and Φ = 1.1. The fuel blend is 21% H_2, 72% NH_3 and 7% N_2 by volume.

The analysis conducted along lines perpendicular to the flame front, as in Fig. 7, is also carried out to analyse the role of thermal diffusion and presented in Fig. 21. The DNS calculations that either include or do not take into account thermal diffusion show similar trends and NO levels and similar correlations to local temperature, mass fraction OH and equivalence ratio. This indicates

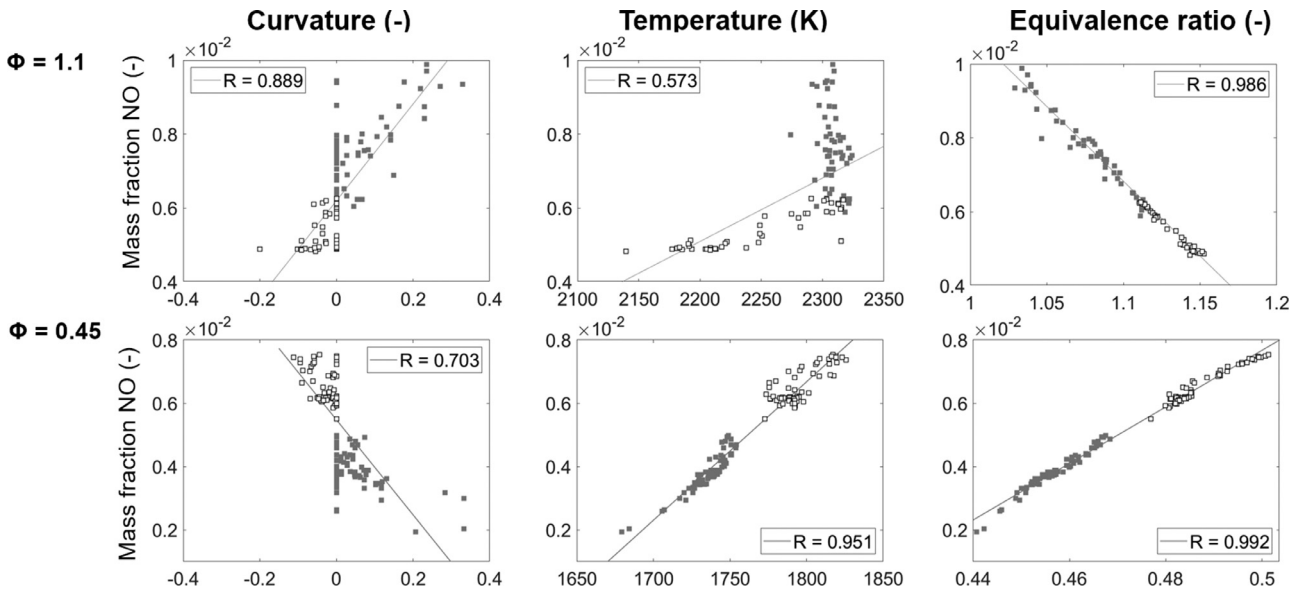

Fig. 19. Local maxima in NO mass fractions, for convex and concave portions of the flame front, versus the corresponding flame curvature, local temperature and equivalence ratio.

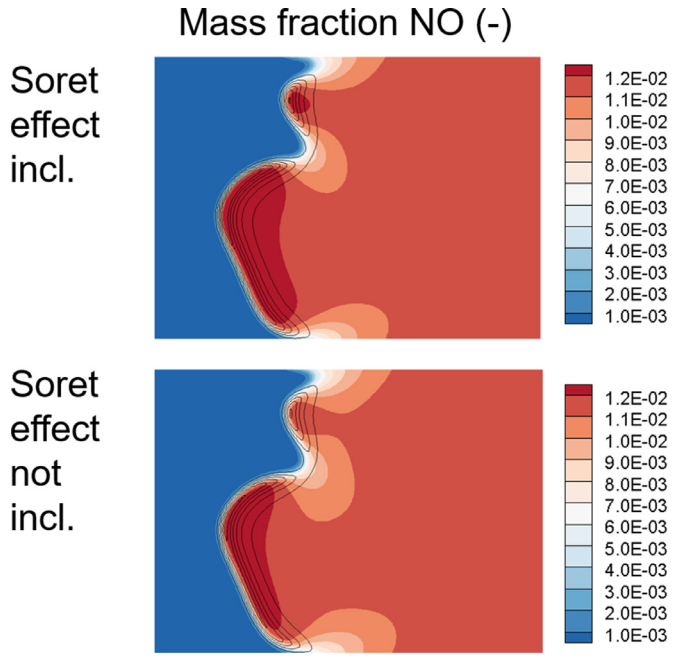

Fig. 20. Contours of NO mass fractions at 1.1 ms for $\Phi = 0.45$. In the upper figure, the Soret effect is included in the numerical model while, in the lower figure, it is not considered.

that the formation of NO, in the vicinity of curved flame portions and its maximum concentration, is impacted by preferential diffusion, as discussed above, but the occurrence of thermal diffusion, acting in addition to that, expands these diffusive effects towards less curved parts of the flame, and further downstream, by driving additional hydrogen into the critical flame regions. These observations support the findings discussed earlier; that fast diffusion of hydrogen species, enhanced by flame curvature and the resulting enrichment or fall-off in local equivalence ratio dominate the level and the location of NO formation, while thermal effects as thermal diffusion and thermal NO formation, reinforce these effects.

4. Conclusions

Two-dimensional DNS with detailed chemical kinetics has been employed to understand the fundamental reaction-diffusion processes leading to the formation of NO in $NH_3/H_2/N_2$-air wrinkled laminar premixed flames. The fast diffusion of H_2 (preferential compared to other species) into convex-shaped portions of the flame front leads to a local increase in equivalence ratio. This change in local equivalence ratio is found to prominently affect the NO formation. If the fuel-air mixture is globally lean, the local increase in equivalence ratio strengthens the formation of the NO species; if the fuel-air mixture is globally rich it will weaken the NO formation process. The decomposition of NH_2 is governed by two competing pathways: the decomposition via NH and N to N_2 on the one hand and the oxidation via HNO to NO on the other hand. The local radical pool, which is affected by preferential diffusion of H_2 and depletion of O_2, and the local fuel-air mixture ratio jointly strengthen further local differences between H_2-depleted (concave) portions of the flame front and H_2-enriched (convex) ones.

Lean conditions have been found to be more sensitive to fuel NO. The more fuel is available and the higher is the adiabatic flame temperature, the more NO forms. At rich conditions, the available oxidizer is the limiting factor in respect the NO formation. The local degradation in equivalence ratio in concave-shaped flame portions, towards stoichometric conditions, leads to a higher NO formation, and H_2 presence favours the direct N_2 formation pathways. Slightly lean conditions ($\Phi = 0.9$) is found to follow the same trend as rich mixture since the maximum NO formation is at $\Phi = 0.8$ and due to depletion of O_2 in convex-shaped sections of the flame front.

All these consideration are useful, at the design stage of combustion systems, in order to select the optimal equivalence ratio or the optimal sequence of equivalence ratios in staged systems, as well as to minimizes NO emissions from equipment burning NH_3/H_2 fuel blends. Although chemical reactions in practical combustion devices (gas turbines and reciprocating engines) typically take place at pressurized conditions, the present results obtained at atmospheric pressure conditions are indicative of analogous local trends and spatial patterns also observed at higher pressures in preliminary investigations (not shown here). Further research will

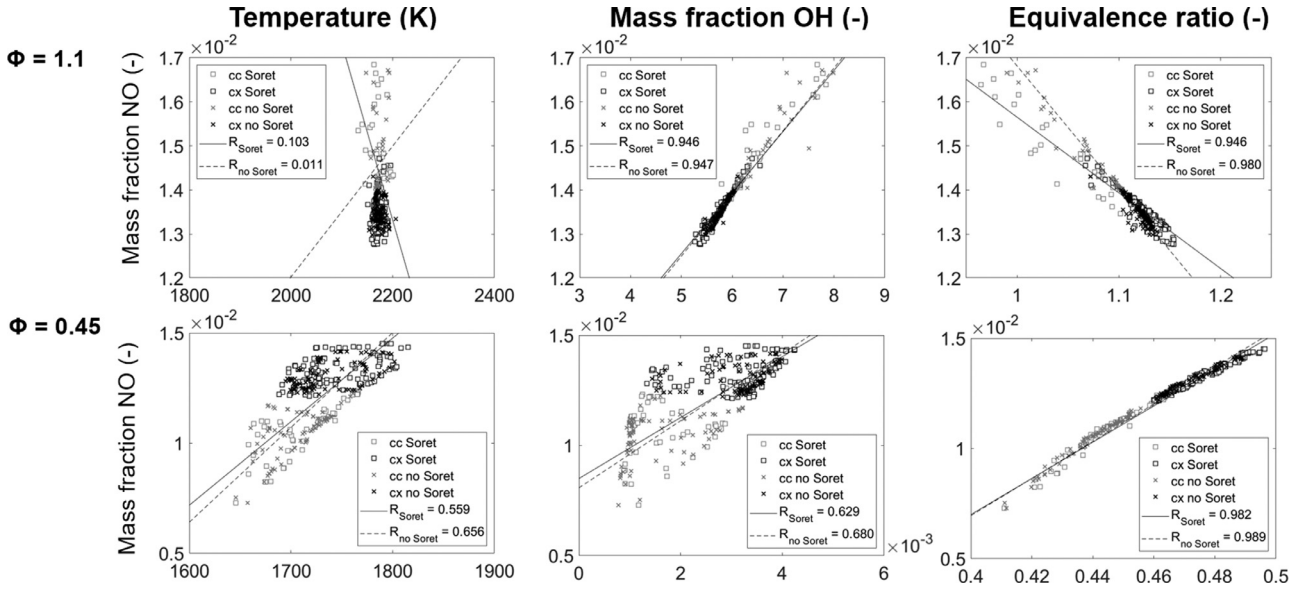

Fig. 21. Local maxima in NO mass fractions, for convex and concave portions of the flame front, versus local temperature, OH mass fraction and equivalence ratio. Squares: Soret effect included. Crosses: Soret effect not included.

systematically address the pressure scaling effect on the NO formation patterns described in the present work and investigate the role of turbulence-chemistry interaction.

Declaration of Competing Interest

The authors declare that they have no known competing financial interests or personal relationships that could have appeared to influence the work reported in this paper.

Acknowledgments

The present research is funded by the CLIMIT-Demo program of the Research Council of Norway, Project Number 617137 (BIGH2/Phase III), Siemens Energy AG, Equinor ASA. Computational resources are provided by UNINETT Sigma2 Project Number nn9527k and Norstore Project Number ns9121k. Furthermore we kindly acknowledge the financial and collaborative support of the CCRC, KAUST.

Appendix A

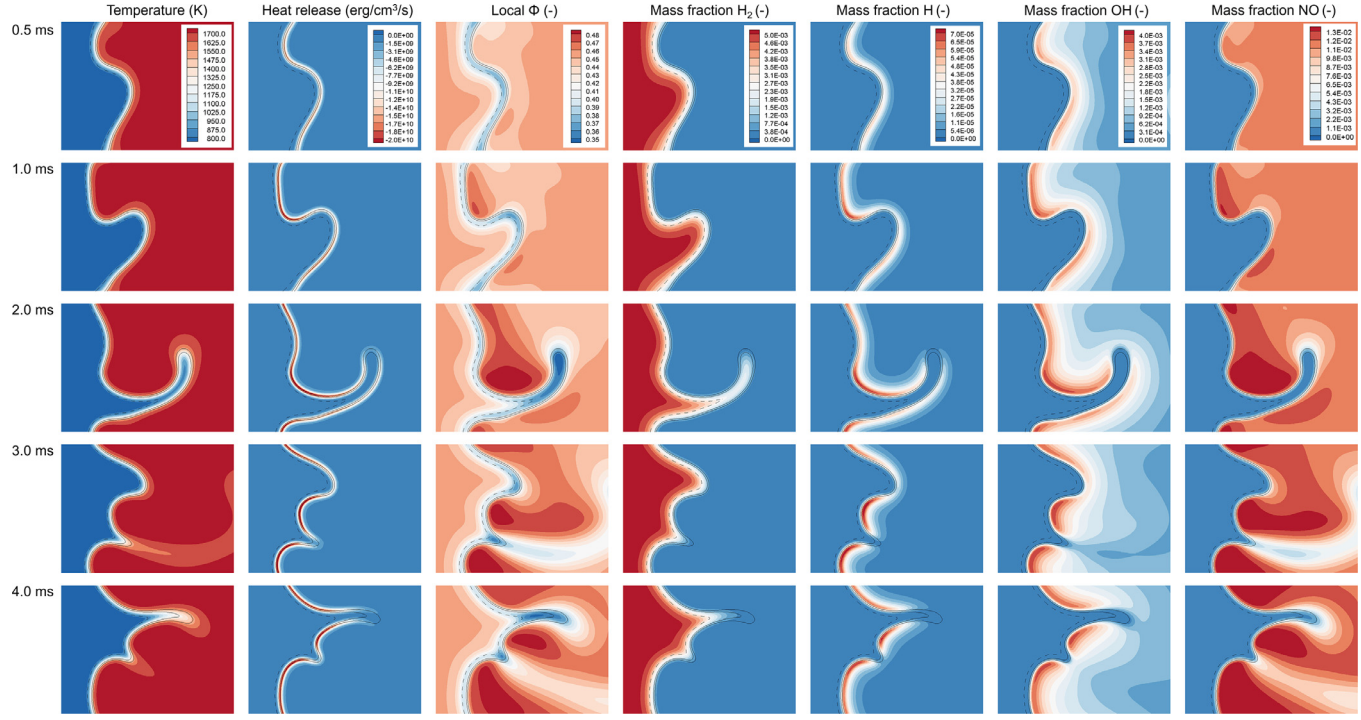

Fig. A1. Temporal of the predicted flame using DNS for $\Phi = 0.45$. Contours of temperatures,heat release, local equivalence ratio, mass fractions H_2, H, OH and NO are shown from left to right. Dashed lines denote the preheated layer ($C = 0.1$), solid black lines the combustion zone ($0.6 < C < 0.8$).

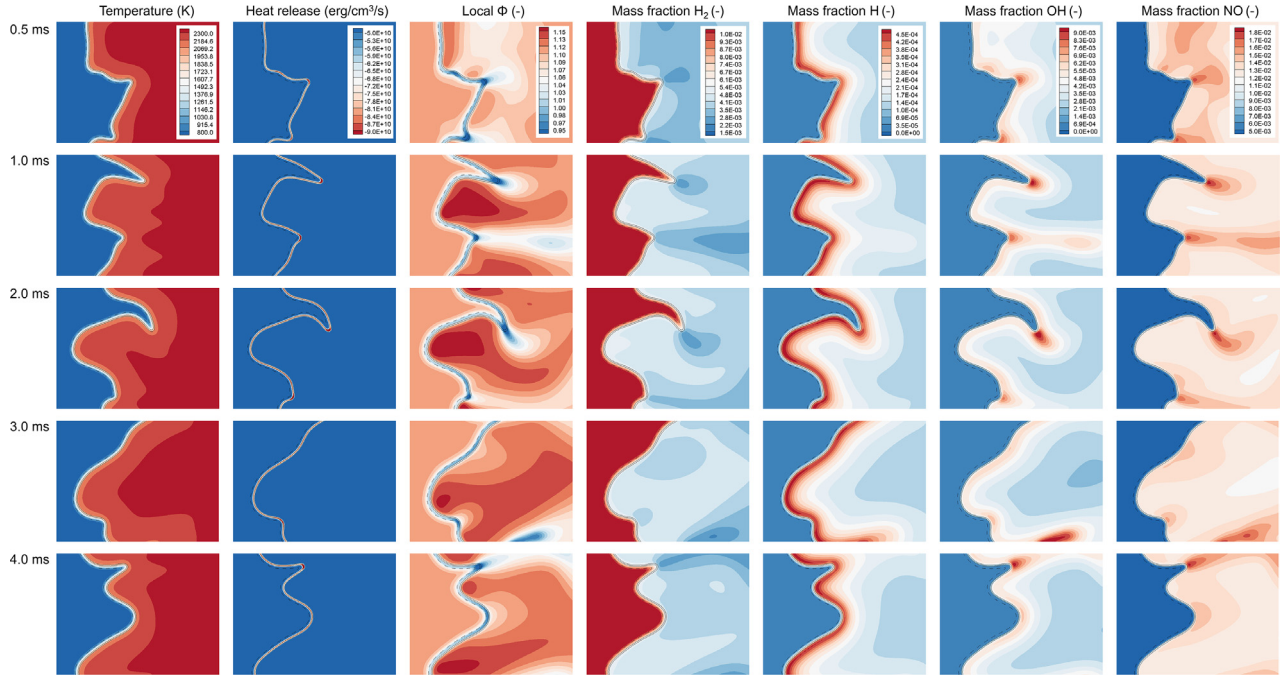

Fig. A2. Temporal of the predicted flame using DNS for $\Phi = 1.1$. Contours of temperatures, heat release, local equivalence ratio, mass fractions H_2, H, OH and NO are shown from left to right. Dashed lines denote the preheated layer (C = 0.1), solid black lines the combustion zone ($0.6 < C < 0.8$).

References

[1] H.F. Abbas, W.M.A. Wan Daud, Hydrogen production by methane decomposition: a review, Int. J. Hydrogen Energy 35 (3) (2010) 1160–1190.

[2] A. Ursua, L.M. Gandia, P. Sanchis, Hydrogen production from water electrolysis: current status and future trends, Proc. IEEE 100 (2) (2011) 410–426.

[3] J. Fuhrmann, M. Hulsebrock, U. Krewer, Transition to Renewable Energy Systems, D. Stolten and V. Scherer, Wiley-VCH Verlag GmbH & Co. KGaA, p. 691–706.

[4] F. Verkamp, M. Hardin, J. Williams, Ammonia combustion properties and performance in gas-turbine burners, Symposium (International) on Combustion, 11, Elsevier (1967), pp. 985–992.

[5] J. Li, H. Huang, N. Kobayashi, Z. He, Y. Nagai, Study on using hydrogen and ammonia as fuels: combustion characteristics and nox formation, Int. J. Energy Res. 38 (9) (2014) 1214–1223.

[6] R. Li, A.A. Konnov, G. He, F. Qin, D. Zhang, Chemical mechanism development and reduction for combustion of $NH_3/H_2/CH_4$ mixtures, Fuel 257 (2019) 116059, doi:10.1016/j.fuel.2019.116059.

[7] A. Valera-Medina, H. Xiao, M. Owen-Jones, W. David, P. Bowen, Ammonia for power, Prog. Energy Combust. Sci. 69 (2018) 63–102.

[8] H. Kobayashi, A. Hayakawa, K. Somarathne, E. Okafor, Science and technology of ammonia combustion, Proc. Combust. Inst. 37 (1) (2019) 109–133, doi:10.1016/j.proci.2018.09.029.

[9] P. Sabia, M.V. Manna, A. Cavaliere, R. Ragucci, M. de Joannon, Ammonia oxidation features in a Jet Stirred Flow Reactor. The role of NH_2 chemistry., Fuel 276 (2020) 118054, doi:10.1016/j.fuel.2020.118054.

[10] G. Sorrentino, P. Sabia, P. Bozza, R. Ragucci, M. de Joannon, Low-nox conversion of pure ammonia in a cyclonic burner under locally diluted and preheated conditions, Appl. Energy 254 (2019) 113676, doi:10.1016/j.apenergy.2019.113676.

[11] K.D.K.A. Somarathne, S. Hatakeyama, A. Hayakawa, H. Kobayashi, Numerical study of a low emission gas turbine like combustor for turbulent ammonia/air premixed swirl flames with a secondary air injection at high pressure, Int. J. Hydrogen Energy 42 (44) (2017) 27388–27399, doi:10.1016/j.ijhydene.2017.09.089.

[12] E.C. Okafor, K.A. Somarathne, A. Hayakawa, T. Kudo, O. Kurata, N. Iki, H. Kobayashi, Towards the development of an efficient low-nox ammonia combustor for a micro gas turbine, Proc. Combust. Inst. 37 (4) (2019) 4597–4606, doi:10.1016/j.proci.2018.07.083.

[13] Y. Jiang, A. Gruber, K. Seshadri, F.A. Williams, An updated short chemical-kinetic nitrogen mechanism for carbon-free combustion applications, Int. J. Energy Res. 44 (2) (2020) 795–810.

[14] J.H. Chen, A. Choudhary, B. de Supinski, M. DeVries, E.R. Hawkes, S. Klasky, W.K. Liao, K.L. Ma, J. Mellor-Crummey, N. Podhorski, R. Sankaran, S. Shende, C.S. Yoo, Terascale direct numerical simulations of turbulent combustion using s3d, Comput. Sci. Discov. 2 (2009) 1–31.

[15] J.H. Chen, T. Echekki, W. Kollmann, The mechanism of two-dimensional pocket formation in lean premixed methane-air flames with implications to turbulent combustion, Combust. Flame 116 (1999) 15–48.

[16] J.H. Chen, H.G. Im, Stretch effects on the burning velocity of turbulent premixed hydrogen/air flames, Proc. Combust. Inst. 28 (1) (2000) 211–218, doi:10.1016/S0082-0784(00)80213-1.

[17] H.G. Im, J.H. Chen, Preferential diffusion effects on the burning rate of interacting turbulent premixed hydrogen-air flames, Combust. Flame 131 (2002) 246–258.

[18] T. Echekki, J.H. Chen, Direct numerical simulation of autoignition in non-homogeneous hydrogen-air mixtures, Combust. Flame 134 (2003) 169–191.

[19] E.R. Hawkes, J.H. Chen, Direct numerical simulation of hydrogen-enriched lean premixed methane-air flames, Combust. Flame 138 (2004) 242–258.

[20] E.R. Hawkes, J.H. Chen, Evaluation of models for flame stretch due to curvature in the thin reaction zones regime, Proceedings 30th International Symposium on Combustion, The Combustion Institute (2005), pp. 647–655.

[21] J.H. Chen, E.R. Hawkes, R. Sankaran, S.D. Mason, H.C. Im, Direct numerical simulation of ignition front propagation in a constant volume with temperature inhomogeneities i. fundamental analysis and diagnostics, Combust. Flame 145 (2006) 128–144.

[22] E.R. Hawkes, R. Sankaran, P.P. Pébay, J.H. Chen, Direct numerical simulation of ignition front propagation in a constant volume with temperature inhomogeneities: ii. parametric study, Combust. Flame 145 (1) (2006) 145–159.

[23] V. Akkerman, V. Bychkov, L.-E. Eriksson, Numerical study of turbulent flame velocity, Combust. Flame 151 (3) (2007) 452–471.

[24] C.A. Kennedy, M.H. Carpenter, Several new numerical methods for compressible shear-layer simulations, Appl. Numer. Math. 14 (0) (1994) 397–433.

[25] C.A. Kennedy, M.H. Carpenter, R.M. Lewis, Low-storage, explicit Runge-Kutta schemes for the compressible Navier-Stokes equations, Appl. Numer. Math. 35 (0) (2000) 177–219.

[26] T. Poinsot, S.K. Lele, Boundary conditions for direct simulations of compressible viscous flow, J. Comput. Phys. 101 (1992) 104–129.

[27] J.C. Sutherland, C.A. Kennedy, Improved boundary conditions for viscous, reactive, compressible flows, J. Comput. Phys. 191 (2003) 502–524.

[28] A. Kundu, Combustion Characteristics of a Swirl Dry Low Emission Burner Concept for Gas Turbine, Lund University, 2016 Doctoral thesis.

[29] M. Nakahara, H. Kido, A Study of the Premixed Turbulent Combustion Mechanism Taking the Preferential Diffusion Effect into Consideration, Technical Report, Department of Mechanical Engineering, Kyushu University, Fukuoka, Japan, 1998.

[30] LOGEresearch 1.10-000, 2018.

[31] K.P. Shrestha, L. Seidel, T. Zeuch, F. Mauss, Detailed kinetic mechanism for the oxidation of ammonia including the formation and reduction of nitrogen oxides, Energy Fuels 32 (10) (2018) 10202–10217, doi:10.1021/acs.energyfuels.8b01056.

[32] J. Otomo, M. Koshi, T. Mitsumori, H. Iwasaki, K. Yamada, Chemical kinetic modeling of ammonia oxidation with improved reaction mechanism for ammonia/air and ammonia/hydrogen/air combustion, Int. J. Hydrogen Energy 43 (5) (2018) 3004–3014, doi:10.1016/j.ijhydene.2017.12.066.

[33] P. Glarborg, J.A. Miller, B. Ruscic, S.J. Klippenstein, Modeling nitrogen chemistry in combustion, Prog. Energy Combust. Sci. 67 (2018) 31–68, doi:10.1016/j.pecs.2018.01.002.